A Full-Field Modular Gamma Camera

T. D. Milster, J. N. Aarsvold, H. H. Barrett, A. L. Landesman, L. S. Mar, D. D. Patton, T. J. Roney, R. K. Rowe, and R. H. Seacat III

Optical Sciences Center, Program in Applied Mathematics, Department of Radiology, University Medical Center, and Department of Electrical and Computer Engineering, University of Arizona, Tucson, Arizona

A modular gamma ray camera is described that gives useful image information over its entire crystal face. The lack of dead area on the periphery of the camera is made possible by a unique application of digital electronics and optimal position estimation using maximum likelihood (ML) estimates. The ML estimates are calculated directly from photomultiplier tube responses and stored in a lookup table, so the restriction of calculating the position estimates in separate circuitry is removed. Each module is designed to be optically and electronically independent, so that many modules can be combined in a large system. Results from a prototypical module, which has an active crystal area of 10 cm × 10 cm, are presented.

J Nucl Med 1990; 31:632–639

We describe an alternative to a standard gamma camera called a modular camera, which is, in essence, a small Anger camera (*1*). Components of the module include a square scintillation crystal, an exit window, and an array of four photomultiplier tubes (PMTs), as shown in Figure 1. The crystal measures 10 cm × 10 cm, which is also the useful field of view for the module. The full field of view is due to a unique application of digital electronics and optimal position estimation, which includes direct analog-to-digital conversion of the PMT responses, a lookup table for position estimation, and an image memory that accumulates the position estimates $\hat{x}$ and $\hat{y}$ (*2*). The lookup table removes the restriction of calculating the estimates in separate circuitry, and we show that it works well over the entire area of the crystal. The direct conversion of analog PMT signals to digital signals was applied to Anger cameras by Genna et al. (*3*) in 1982, but $\hat{x}$ and $\hat{y}$ estimates were calculated in separate circuitry, and a large planar crystal was used. The modular design concept has been investigated by Muehllehner et al. (*4*), Rogers et al. (*5*) and Rogers et al. (*6*), but none of these systems digitizes the PMT responses directly, and both calculate $\hat{x}$ and $\hat{y}$ in separate circuitry. Burnham et al. (*7*) have discussed a modular system that calculates one position coordinate.

The modular cameras may be used individually, but they are most efficient when used in large systems where count rate is an important specification (*8,9*). For an Anger camera, the count rate is limited because each gamma ray that strikes the large planar crystal must be processed completely before another event can be processed. The modular cameras are designed to be optically and electronically independent, so the system count rate is N times the count rate of one module, where N is the number of modules in the system.

In this paper, we describe the theory of position estimation in the modular cameras and the hardware associated with implementing the theory. Procedures are described that are used to calibrate the module, and results are presented from a prototypical modular camera.

METHODS

The design of our modular camera presents new challenges that cannot be met by simple extensions of design principles established for Anger cameras. Since we anticipate using these modules in close-packed arrays, it is important that the entire crystal area be useful for imaging. We accomplish a full field of view by implementing a statistical estimator instead of standard sum-and-difference circuitry. Digital electronics and a lookup table are used to realize the estimator in hardware. The contents of the lookup table are calculated in a two-step process. First, a calibration accurately determines PMT responses as a function of scintillation position. Then the lookup table is calculated by using the calibration information and maximum likelihood (ML) estimation rules. This section describes the ML estimate, the signal-processing hardware, the calibration technique, the calculation of the lookup table, and techniques for improving flood-field uniformity.

The Estimation Problem

A scintillation event is specified by the position coordinates (x_0,y_0) of a light flash in a NaI(Tl) crystal. The light flash produces a set of PMT responses, $(n_1n_2n_3n_4)$, where n_i is defined as the number of photoelectrons detected in PMT i during a short time interval. The likelihood of a particular $(n_1n_2n_3n_4)$, for a scintillation event at (x_0,y_0), is given by the statistical properties of the light flash, camera geometry, and PMT characteristics (*10*). It has been argued that the number of photoelectrons from a scintillation flash follows the Poisson probability distribution (*11*), although work by some research-

Received July 18, 1989; revision accepted Nov. 10, 1989.

For reprints contact: Tom D. Milster, PhD, Optical Sciences Center, University of Arizona, Tucson, Arizona 85721.

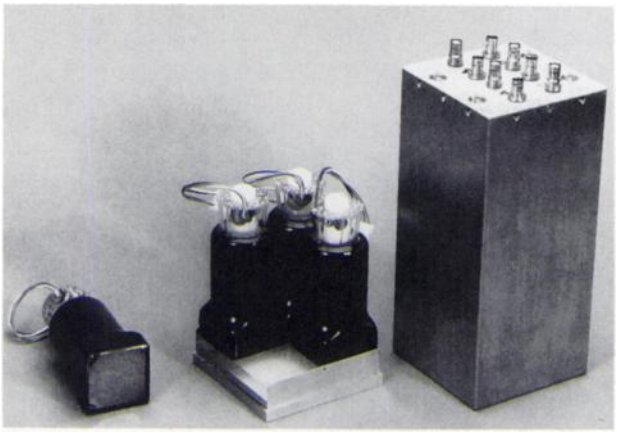

FIGURE 1
Modular camera optical components. Four square PMTs view a 10 cm × 10 cm (NaI(Tl) crystal through a 19.0-mm thick exit window. The assembly is covered by an aluminum housing when in use.

ers indicates that it is slightly non-Poisson (*12*). In this report, we assume that the signals from the PMTs are independently Poisson distributed, that is:

$$P(n_1n_2n_3n_4 \mid xy) = \prod_{i=1}^{4} P(n_i \mid xy) = \prod_{i=1}^{4} \frac{f_i^{n_i} \exp[-f_i]}{n_i!}. \quad (1)$$

The function $f_i(x,y)$ is the mean detector-response function (MDRF) for PMT i and event position (x,y), that is:

$$f_i(x,y) = \langle n_i(x,y) \rangle, \quad (2)$$

where the brackets denote the statistical average. We also have investigated other techniques for which the Poisson assumption is not necessary (*13*), but no significant improvement in camera performance was found. Note that we do not assume the dependence of $f_i(x,y)$ on x and y is separable.

During the operation of scintillation cameras, PMT responses are processed as they occur to obtain position estimates. Conventional scintillation cameras use a resistive or capacitive network to provide sum and difference signals that are combined to yield position estimates. In the center of the crystal, where the MDRFs are approximately linear, sum-and-difference circuitry works well. Toward the edges of the crystal and near the tube centers, the MDRFs become nonlinear, which leads to position errors in the estimates (*14*). In commercial systems, postcorrection schemes are commonly used to correct small position errors, but the position errors near edges of the crystal are so large that they cannot be easily corrected. Instead, this dead area is simply masked and not used.

We initially used sum and difference circuitry in our modular cameras, but the resulting dead area was a significant portion of the crystal area (*15*). In order to obtain accurate position estimates over the entire crystal area, we implemented an ML estimator, which is the (x,y) value that maximizes $P(ABCD|xy)$ for a particular ABCD, where A, B, C and D are the signal levels after the n_1, n_2, n_3 and n_4 photoelectrons, respectively, are processed by the electronics. We also investigated a minimum-mean-square-error (MMSE) estimator and found that it performed similarly to the ML estimator in a one-dimensional modular camera (*15*).

The use of statistical methods for finding position estimates in scintillation cameras has been investigated by other researchers. For example, Gray and Macovski (*16*) suggested the use of the maximum *a posteriori* (MAP) estimate, which is equivalent to the ML estimate if all (x,y) positions in the crystal area equally likely. Also, Clinthorne et al. (*17*) described an ML position computer for use in position-sensitive detectors.

Hardware

The signal processing for the modular camera is divided into six stages: acquisition, conversion, compression, estimation, accumulation, and post-processing. A flow diagram of the signal processing is displayed in Figure 2. In the first stage, the light flash from a scintillation event produces electrical

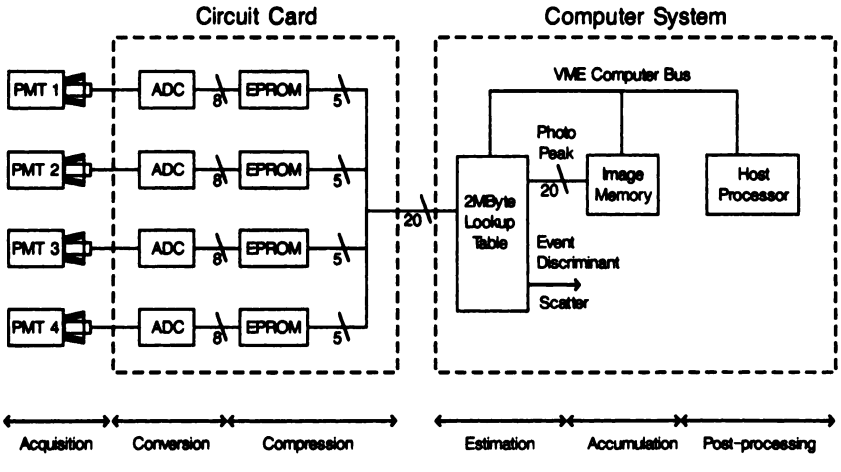

FIGURE 2
Flow diagram of the modular camera signal processing. The light from a scintillation event is first acquired by the PMTs. The analog signals are digitized by eight-bit analog-to-digital converters (ADCs) and compressed into five-bit digital signals with erasable programmable read-only memories (EPROMS). Signals from the four EPROMs are combined into a twenty-bit address to a lookup table where position estimates are stored. If the EPROM signals correspond to a photopeak event, the position estimate is accumulated in an image memory. After data collection is completed, the host processor can be used to apply image processing techniques, such as smoothing or tomographic reconstruction, to the data. The conversion and compression hardware is located on a special-purpose circuit card, and the estimation, accumulation, and post-processing is performed on a dedicated computer system.

current pulses in the four PMTs corresponding to a particular response ($n_1n_2n_3n_4$). The second stage converts the electrical pulses into digital signals. The next two stages, compression and estimation, process the digital information to estimate the position of the scintillation in the crystal. The fifth stage, accumulation, produces an image of the gamma flux incident on the crystal face by accumulating position estimates in an image memory. The last stage, post-processing, is utilized if an image-processing technique, such as smoothing or tomographic reconstruction, is required. The hardware is organized so that the conversion and compression stages are located on a special-purpose circuit card. The estimation, accumulation, and post-processing stages reside in a computer system. The host processor communicates with the image memory and the lookup table over a standard VME computer bus. The following paragraphs describe the hardware of each stage in more detail.

The acquisition-stage hardware consists of the PMTs and analog filters. After a scintillation event occurs in the crystal, photoelectrons are generated by the photocathodes of the PMTs. The resulting current pulses from the output of the PMT dynode chains arrive at passive shaping filters via coaxial cables. The pulses are integrated with a time constant of ~0.8 μsec. The filters are followed by two stages of active gain, resulting in an amplification factor of ~500.

The conversion-stage hardware consists of four analog-to-digital converters (ADCs), which convert the acquisition-stage analog signals. We initially constructed the modular camera using five-bit quantization in each ADC, which resulted in unsatisfactory images (*13*). Figure 3A shows an image of a thyroid phantom taken through a high-resolution collimator using five-bit quantization in each ADC. Artifacts from the quantization appear in a band surrounding the phantom. In order to improve the quality of the image, the number of quantization levels was increased. We now use eight-bit quantization in each ADC.

The lookup-table memory size for five-bit quantization is 2^{20} words or two megabytes (five bits from each ADC, four ADCs, and one word of memory per location), which is an easily obtainable amount of memory given state-of-the-art computer products. For eight-bit quantization, the lookup-table memory size would be 2^{32} words or four gigabytes, which is a prohibitive amount of computer memory. Instead of implementing such a large lookup table, we compress the eight-bit digital information into five-bit digital signals.

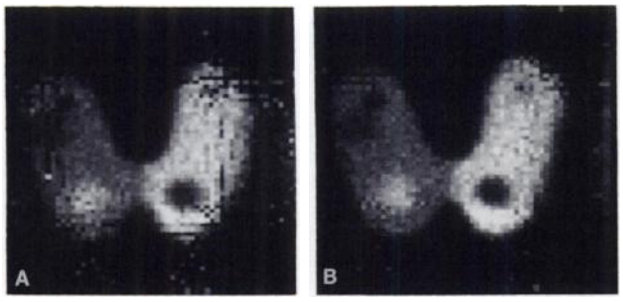

FIGURE 3
Thyroid phantom images taken through a high-resolution collimator. (A) Image acquired by a system using an EPROM set so as to perform a linear eight-bit to five-bit mapping. A small air bubble is present in the upper left corner of the phantom, but because of the quantization artifacts, it is not easily discernible. (B) Image acquired by the same system used in Figure 3A after the EPROM setting was changed so as to perform an approximate square root eight-bit to five-bit mapping. The phantom's position was unchanged. Images A and B are the result of dividing by a reference flood image.

The compression-stage hardware consists of four erasable, programmable read-only memories (EPROMs), one for each ADC. The eight-bit signals from the ADCs are used as addresses to the EPROMs. The contents of the addressed locations correspond to the square roots of the eight-bit signals. For example, consider the EPROM corresponding to PMT A. The contents of the EPROM are:

$$A = \sqrt{a},$$

where a is the eight-bit input signal (the digital address to the EPROM) and A is the five-bit output signal (the contents of the addressed location). The four compressed output signals, A, B, C and D, are combined to form a 20-bit address for the lookup table. Figure 3B shows an image of the thyroid phantom using eight-bit quantization on the ADCs and square-root compression circuitry; quantization artifacts are greatly suppressed.

The estimation stage of the signal processing is simply the lookup table, which is a dedicated portion of computer memory. Each memory location in the lookup table corresponds to a unique combination of A, B, C and D signals. The lookup table is organized so that each addressed location contains one word (16 bits) of information. Twelve bits of the word are used to indicate the $(\hat{x},\hat{y})$ estimate of event position: six bits for the $\hat{x}$ estimate and six bits for the $\hat{y}$ estimate. Three of the remaining bits determine into which of eight possible image memories the position estimate is accumulated. The sixteenth bit is used for discriminating against scattered radiation or other events outside the photopeak. If the *ABCD* does not correspond to a photopeak event, a logical 1 is stored in the sixteenth bit. If the *ABCD* corresponds to a photopeak event, a logical 0 is stored in the sixteenth bit. The procedure for determining if *ABCD* corresponds to a photopeak event is discussed in a later section.

The accumulation stage includes the image memory, which is implemented as additional dedicated memory in the computer and the necessary circuitry to increment the counts in this memory. The image memory is organized as a matrix of 64 × 64 locations, corresponding to the six-bit $\hat{x}$ estimate and the six-bit $\hat{y}$ estimate. A position estimate from the lookup table is accumulated by addressing the proper location in the matrix and adding one to the contents of the location. If the sixteenth bit is a logical 1, the hardware does not accumulate the estimate.

Post-processing takes place in the host processor. After the data are collected in the image memory, special-purpose programs are used to perform image processing functions if such processing is needed or desired.

Calibration Procedure

In order to calculate the ML estimate, the MDRFs should be determined at each of the 4,096 (x,y) locations on the crystal. Analytical solutions for the MDRFs are difficult to obtain because of the large number of phenomena, such as reflection from the packing material surrounding the crystal and reflection from the crystal-window interface, that contribute to the PMT response. Monte-Carlo techniques can predict

the general shapes of the MDRFs as a function of position, but they do not yield correct quantitative results due to the difficulty in determining exact material parameters (*10*). The best method for determining the MDRFs accurately is to measure them directly.

To measure the MDRFs, we start with a collimated point source of technetium-99m (^{99m}Tc), which has a beam width of ~2.0 mm, incident on some location (x_0,y_0) of the crystal. The 20-bit address from the compression stage is used as the address to a large (2^{20} word) computer memory. Each time a location in the large memory is addressed, the contents of that location are incremented by one. When a sufficient number of counts is collected, the data are an approximation of:

$$P(ABCD \mid x_0y_0),$$

where A, B, C and D are the signal levels after the n_1, n_2, n_3 and n_4 photoelectrons, respectively, are converted into voltage signals, digitized, and compressed. We could use these data directly to determine the ML position estimates. The technique involves observing the number of counts collected at each $ABCD$ versus the location of the point source. The (x,y)'s that correspond to the maximum number of counts at each $ABCD$ are the ML estimates. Our results indicate that severe quantization artifacts appear in images produced by this lookup table unless the data are accumulated at each of the 4,096 (x,y) locations (*13*). The amount of time required for data collection and processing at 4,096 (x,y) is prohibitive (~11 hr). If we assume that the MDRFs vary smoothly with position, and if we use more sophisticated estimation methods on a courser grid of points, we can greatly reduce the overall time for calibration of a module.

Our calibration method consists of first estimating the MDRFs from the point-source data, which requires a statistical model for these data. If the n_i are statistically independent, as was assumed to obtain Equation 1, the five-bit digital signals are also statistically independent, that is:

$$P(ABCD|xy) = P(A|xy)\ P(B|xy)\ P(C|xy)\ P(D|xy). \quad (3)$$

Even if we assume that the photoelectrons ($n_1n_2n_3n_4$) obey Poisson statistics, the $ABCD$ do not. Instead, given our assumptions, they are well modeled as binned Poisson distributions with appropriate correction for nonlinear data compression. Figure 4 illustrates the transformation of $P(n_1|xy)$ by a square-root mapping. This mapping transforms a Poisson random variable to one with approximately constant variance (*18*).

After the $ABCD$ data are collected for one location of the point source, the MDRFs for that location are determined from the data by an ML estimation procedure called logarithmic matched filtering (*18*). In this method, the data are processed to obtain $\{M_{ki}\}$, where M_{ki} is the number of events recorded in bin k (k = 0, ..., 31) corresponding to PMT i (i = 1,2,3,4). The $\{M_{ki}\}$ approximate the signal probability distributions of each PMT. For example, $\{M_{ki}\}$ approximates $P(A|x_0y_0)$. The ML estimate of $fi(x_0,y_0)$ given $\{M_{ki}\}$ is obtained by maximizing the appropriate likelihood function, $P(\{M_{ki}\}|f_i(x_0,y_0))$. It can be shown (*19*) that maximizing $P(\{M_{ki}\}|f_i(x_0,y_0))$ is equivalent to maximizing:

$$\sum_{k=0}^{31} M_{ki} \ln[P(k \mid f_i(x_0,y_0))], \quad (4)$$

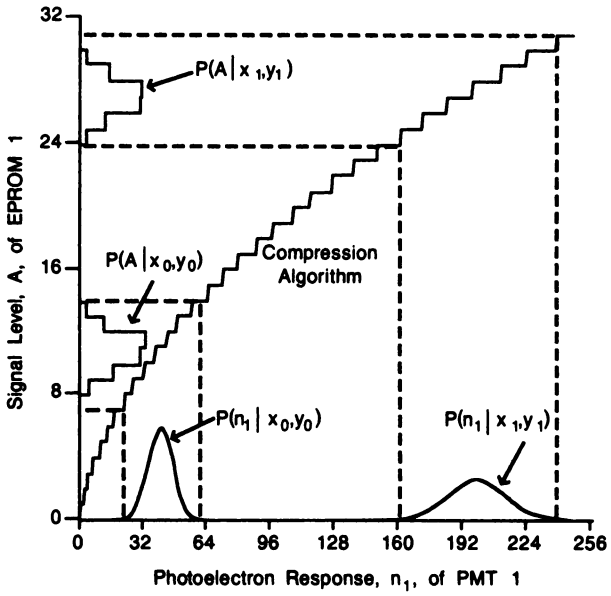

FIGURE 4
Transformation of $P(n_1|x,y)$ into $P(A/x,y)$. The Poisson probability distribution for n_1 is shown for two locations on the crystal, (x_0,y_0) and (x_1,y_1). These distributions are mapped into $P(A|x_0y_0)$ and $P(A|x_1y_1)$ by the binning and nonlinear compression algorithm. The variance of $P(n_1|xy)$, which is indicated by the width of the distribution in the figure, changes with (x,y). The variance of $P(A|xy)$ is nearly uniform with (x,y).

where $P(k|f_i(x_0,y_0))$ is the probability that a scintillation event at (x_0,y_0) will yield a count in the kth bin corresponding to tube i. The distribution $P(k|f_i(x_0,y_0))$ is not exactly Poisson because of the binning and the nonlinear compression, but it is easily calculated. Note that Equation 4 is a weighted sum of the data, $\{M_{ki}\}$. We calculate and store the weights, the values of $\ln[P(k|f_i(x_0,y_0))]$, for values of $f_i(x,y)$ ranging from 0 to 32 in increments of 1/32, that is, for 32 increments of each bin. These stored data represent 1,024 possible estimates of $f_i(x,y)$. We then "match" the data to the optimal stored estimate by maximizing Equation 4 over the stored distributions of weights.

The MDRFs are routinely measured at every fourth location in each direction, which results in a 16 × 16 sampling of the (x,y) locations. After the MDRF values are determined at these sample points, an interpolation method is used to determine the MDRF values at the remaining (x,y) locations. We have tried using linear and bicubic spline interpolation, but quantization artifacts were evident in the images. The method we have found satisfactory is to Fourier transform the sampled values, filter in the spatial-frequency domain, and transform back to the spatial domain. The result is a 64 × 64 MDRF array that significantly reduces the quantization artifacts in the images.

Lookup Table Calculation

We now describe how the ML estimate is calculated for a particular $A_0B_0C_0D_0$, that is, for one address in the lookup table. First, the signal probability distributions, for example $P(A_0|xy)$, are calculated using the MDRFs determined in the calibration. Quantization due to the ADCs is accounted for by integrations over small intervals of n_i in Equation 1. For

eight-bit quantization, the intervals are 1/256 of the ADC range. Appropriate correction is then applied for the nonlinear data compression and binning to yield $P(A_0|xy)$, etc. Then the product of the signal probability distributions is calculated to yield $P(A_0B_0C_0D_0|xy)$, as shown in Equation 3, and (x,y) space is searched to obtain the maximum of $P(A_0B_0C_0D_0|xy)$. The (x,y) that maximizes $P(A_0B_0C_0D_0|xy)$ is the ML estimate $(\hat{x},\hat{y})$ corresponding to $A_0B_0C_0D_0$. Finally, we apply a procedure called "likelihood windowing" to determine if the estimate corresponds to a photopeak event. The following paragraphs describe the search procedure and the windowing in more detail.

The search over (x,y) space can be accomplished in several ways. A brute force method for finding the ML estimate is to calculate the likelihoods for all (x,y) for each address in the lookup table, but this would be extremely time consuming. In order to reduce the computation time, we implement a nested-search routine that capitalizes on the assumed statistical independence of the individual signals.

The area of (x,y) space that exhibits a $P(A_0|xy)$ above a predetermined threshold T_{ns} (where ns stands for nested search) is determined by an exhaustive search in (x,y) space. This area, denoted S_1, corresponds to the crystal area where A_0 is probably due to a photopeak scintillation event. The S_1 area is exhaustively searched to find another area S_2 where $P(B_0|xy) > T_{ns}$. The process is continued for the C_0 and D_0 signal values, and the result is a small area S_4 that corresponds to the logical AND of the four threshold conditions. The S_4 area, which is much smaller than the original (x,y) space, is then exhaustively searched for the ML estimate $(\hat{x},\hat{y})$. If the resulting S_4 area has zero net area, $A_0B_0C_0D_0$ is probably not due to a photopeak event. In this case, the content of the lookup table corresponding to $A_0B_0C_0D_0$ is tagged to indicate a nonphotopeak response, that is, a logical 1 is set in the sixteenth bit of the addressed location, as explained in a previous section.

As in commercial gamma cameras, the image quality of the modular cameras is improved by using a windowing procedure. Ordinarily, the energy signal E, the sum of the PMT signals, would be used to discriminate between photopeak and nonphotopeak events. A range of E around the average energy signal, $\langle E \rangle$, defines the bounds of acceptable E. In the modular camera, however, E is a function of position, $E = E(x,y)$, and the established methods of energy windowing are difficult to apply. Instead, we use likelihood windowing, a technique that windows the lookup table according to the likelihood that $A_0B_0C_0D_0$ resulted from a photopeak event. If S_4 has nonzero net area, $P(A_0B_0C_0D_0|\hat{x}\hat{y})$ is compared to another threshold value, T_{lw} (where l^w stands for likelihood window). If $P(A_0B_0C_0D_0|\hat{x}\hat{y}) > T_{lw}$, $A_0B_0C_0D_0$ is assumed to have resulted from a photopeak event and the estimate $(\hat{x},\hat{y})$ is considered valid. If $P(A_0B_0C_0D_0|\hat{x}\hat{y}) < T_{lw}$, $A_0B_0C_0D_0$ probably did not result from a photopeak event, and the content of the lookup table corresponding to $A_0B_0C_0D_0$ is tagged to indicate a nonphotopeak response. We call this technique likelihood windowing because the likelihood function $P(ABCD|\hat{x}\hat{y})$, rather than the total energy, is the criterion for discrimination of photopeak and nonphotopeak events.

Uniformity Correction

The uniformity of a flood image is an important specification for gamma cameras. A raw (not post-processed) image of a flood source is shown in Figure 5A. The brightness of each pixel corresponds to the number of counts recorded in it. This pattern is almost uniform near the center of the crystal, but alternate bright and dark pixels are observed near the edges and especially in the corners. The uniformity of the flood image can be improved by using several methods that we describe in the following paragraphs.

One method for improving the uniformity is to modify the ML estimates in the lookup table. A data set is collected that is similar to the ones collected in the calibration procedure, except that a flood source is used. The lookup table is stored in computer memory, and the computer constructs an image from the data set and the lookup table. An average gray level in this flood image is computed, and, of course, some of the pixels are darker than the average and some are brighter. The modified ML approach to flood correction is to reassign some $ABCD$ values from their true ML values to neighboring pixels if, by doing so, we reduce the number of counts in a bright pixel and increase the number in a darker pixel. In no case do we change the position estimate by more than one pixel from

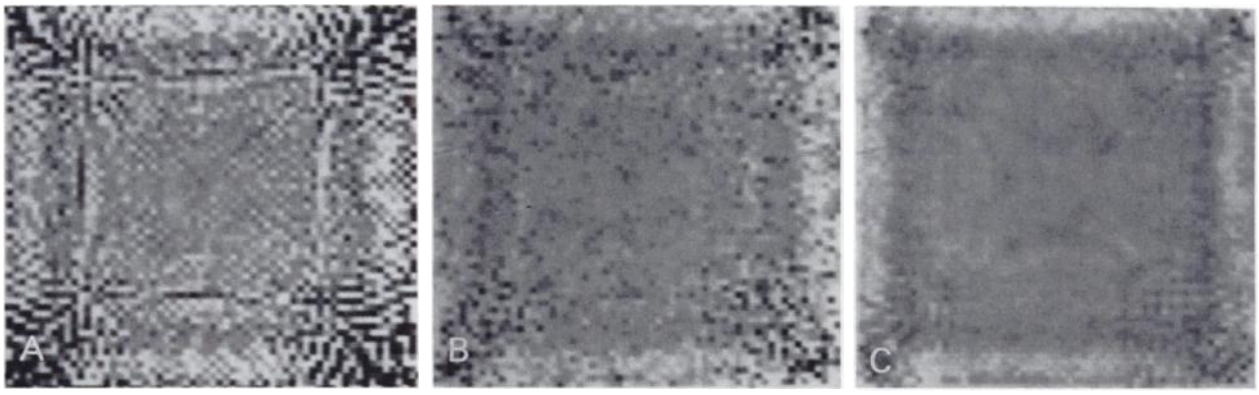

FIGURE 5
Flood images. (Left panel) A raw (not post-processed) image of a flood source. (Middle panel) An image of a flood source using the modified ML lookup table. (Right panel) An image of a flood source using a multiple assignment technique. For all three images, the digital data were displayed on a linearized monitor for which the displayed luminance was rigorously proportional to the digital value. The photographic process, however, increases the contrast so that relatively subtle nonuniformities are evident on the figures.

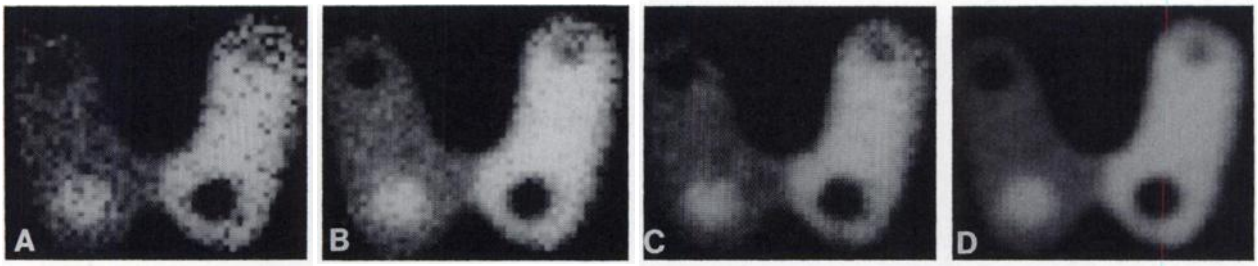

FIGURE 6
Thyroid phantom images processed with different uniformity-correction techniques. (A) An image of a thyroid phantom using a modified ML lookup table. (B) Data of Figure 5A divided by a reference flood image. (C) An image of a thyroid phantom using a multiple-assignment technique. (D) Data of Figure 5C divided by a reference flood image.

its true ML value, so the effect of this reassignment on spatial resolution is minimal.

In deciding which *ABCD* locations to reassign, we first search the flood image for pixels brighter than the average which have neighbors darker than the average. These *ABCD*s are candidates for reassignment. The candidates are ranked in decreasing order of their likelihoods, calculated on the *new* location. These candidates are then reassigned in order until no further improvement in flood uniformity would result. The modified ML lookup table can now be used in place of the ML lookup table for collecting images, and significantly better flood images are obtained as shown in Figure 5B.

The flood nonuniformities are almost completely eliminated by extending the idea in the preceding paragraph. A data set is collected using the technique outlined in the calibration procedure with a flood source. After the exposure is finished, the computer calculates the image directly from the likelihood function. For each *ABCD* in the data set, a nested search of (x,y) space is performed in order to find a small area in which the likelihood is above a predetermined threshold value. A number of counts proportional to the product of the counts in *ABCD* and the likelihood is added to each pixel in the image that lies within the search area. In this way, we do not assign an *ABCD* to just one pixel, but rather to several in proportion to their likelihoods. This approach, which we refer to as multiple assignment, results in a very smooth flood image, as shown in Figure 5C. However, the time required to produce an image from a data set in this way is too long for real-time image acquisition. The multiple-assignment technique is instructive because it illustrates that the flood-image non-uniformities are associated with the assignment of a single pixel value to each *ABCD*.

The third technique for improving flood-field uniformity is to divide the image data by a reference flood image. This corrects for nonuniformity on a pixel-by-pixel basis. The effects of these three methods of uniformity correction on image quality are illustrated in Figure 6.

EXPERIMENTAL RESULTS

Several modular cameras have been constructed and tested. This report lists results obtained from a modular camera with a 5.0-mm thick crystal of NaI(Tl) in a package designed by Harshaw, Inc, Solon, OH. The total exit window thickness is 19.0 mm with no masking. Four Hamamatsu 5.0-cm square PMTs are coupled to the top of the exit window. Standard PMT voltage dividers produce the dynode voltages, and a multiple-channel, digitally controlled LeCroy high voltage power supply provides voltages for each divider. The following paragraphs discuss the spatial resolution, energy resolution, flood-field uniformity and count rate of this camera.

Spatial resolution of the module was tested by placing a collimated point source of ^{99m}Tc, which had a beam width of ~2.0 mm, at an array of (x,y) locations on the crystal. The array consisted of 64 locations on an 8 × 8 grid. Figure 7 shows an image of an array that was post-processed by dividing the raw image with a reference flood image and filtering with a 3 × 3 median filter. A visual inspection of Figure 7 indicates that the positions of the point images closely correspond to the grid locations. Gross position errors commonly observed in uncorrected images from large Anger cameras are not observed. Near the edges, the shapes of the point

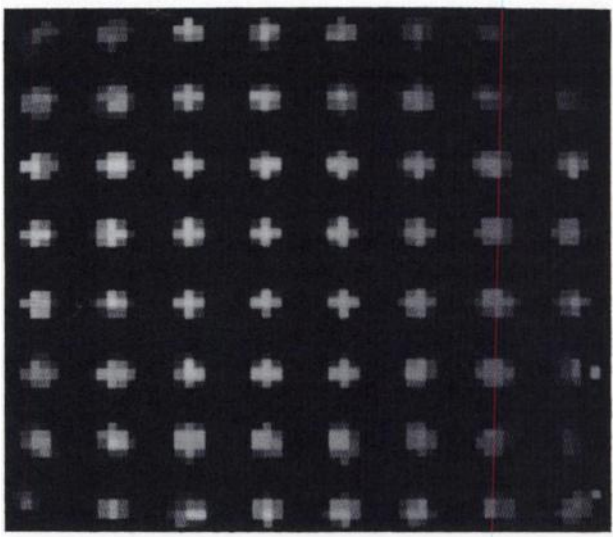

FIGURE 7
Image of a point-source array that has been post-processed by dividing with a reference flood image and by filtering with a 3 × 3 median filter. The array consists of 64 locations on an 8 × 8 grid. Spatial resolution is 3.5 mm FWHM in the center of the crystal, and post-processing to correct position errors is not implemented.

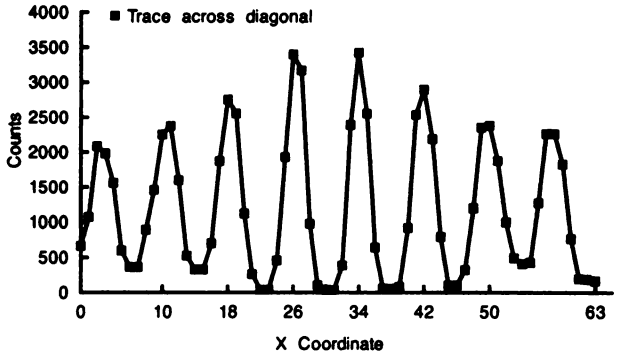

FIGURE 8
Trace across the diagonal of Figure 7.

images become slightly longer in the direction perpendicular to the edge. In the corners, where spatial resolution is poorest, point images are more degraded. Figure 8 is a trace across the diagonal of Figure 7.

Spatial resolution was quantified by observing the number of counts in the center image pixel as the point source moves along a line through the center of the crystal. The point source moved in 1/10 pixel steps. The full-width-at-half maximum (FWHM) spatial resolution was determined by noting the source positions where the maximum and half maximum number of counts occur. For our modular camera, the measured spatial resolution in the center of the crystal is ~3.5 mm FWHM using this technique. If we assume that the 2-mm beam width of the source adds in quadrature to the intrinsic camera resolution, we get 2.8 mm for the latter.

Energy resolution was tested by placing a collimated point source of ^{99m}Tc in the center of the crystal. A multi-channel analyzer was connected to the output of each PMT through a spectroscopy preamplifier, and the energy resolution at FWHM, $\Delta E/E$, was measured. The result was that $\Delta E/E \simeq 20\%$ for each PMT. The energy resolution for the combined signal from the four PMTs was 10%.

Flood-field uniformity was measured by placing a 1.0-mCi point source of ^{99m}Tc approximately 1.0 mm from the face plate of the camera, and nine million counts were collected in the image. At this distance, the maximum intensity difference between the center and the corner is just under 0.5%. To be consistent with specifications from the National Electrical Manufacturers Association (NEMA) (*20*), we defined the pixel size to be 6.3 mm square (4 × 4 array of our standard pixels) for the uniformity measurement. Integral uniformity, defined as [(Max − Min)/(Max + Min)] of the counts collected in NEMA pixels over the entire image, was 15.0% without any uniformity correction. Differential uniformity, defined as [(Max − Min)/(Max + Min)] using a 5 × 1 or 1 × 5 window of NEMA pixels, was 14.6% at the worst-case position in the image. When the flood image was divided by a reference flood image, the integral uniformity was 2.1% and the differential uniformity was 1.3%.

Count rate was measured by placing a point source of ^{99m}Tc in front of the modular camera. A series of lead plates was placed between the source and the crystal, and the count rate was measured as a function of the lead thickness. These data were converted into a graph of observed scintillations versus the true scintillations, as shown in Figure 9. Data for both the unwindowed count rate and the windowed count rate are shown. The windowed count rate includes only those counts which pass through the likelihood window. The maximum windowed count rate for the modular camera is ~120 kcps.

A clinical thyroid image taken with a modular camera is shown in Figure 10. Approximately 20 mCi of pertechnetate was injected intravenously into the subject, and an image was acquired through a high-resolution collimator in contact with the subject's neck. Imaging time was ~10 min.

SUMMARY AND CONCLUSIONS

We have discussed the design and construction of modular scintillation cameras. The hardware for these cameras includes six stages of signal processing: data acquisition, conversion of the PMT responses into eight-bit digital signals, compression of the eight-bit signals into five-bit signals, determination of scintillation position estimates from a digital lookup table, accumulation of the estimates in an image memory, and post-processing of the image data. For these modules, we have developed a calibration procedure used to obtain high-quality MDRFs, which are used to calculate ML position estimates. The lookup table and ML estimation scheme remove the restriction of calculating the $(\hat{x},\hat{y})$ position estimates in separate circuitry. Images of point-source arrays show that the usable

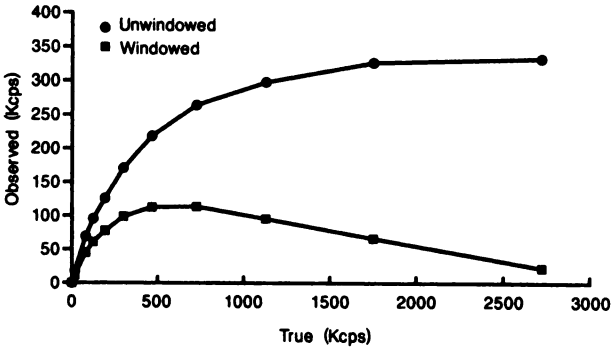

FIGURE 9
Observed scintillations versus true scintillations. The windowed count rate includes only those counts which pass through the likelihood window. The maximum windowed count rate for the modular cameras is ~120 Kcps.

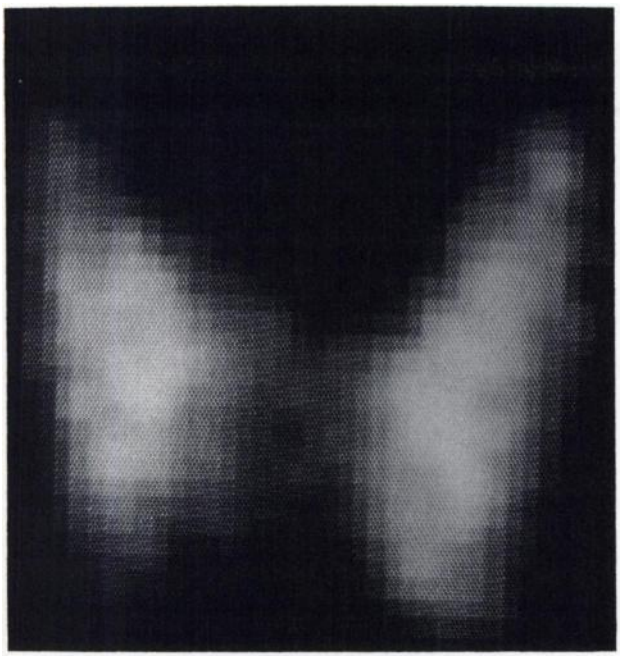

FIGURE 10
A clinical thyroid image taken with a modular camera. Approximately 20 mCi of pertechnetate was injected intravenously into the subject, and the image was acquired for 10 min through a high-resolution collimator in contact with the subject's neck.

field-of-view is essentially the entire crystal area. It is obvious from a visual inspection of the point-source image arrays that the position errors are small compared to the spatial resolution of the camera, so it is not necessary to post-process the data to correct for position errors. The modular camera is characterized by spatial resolution of ~3 mm and energy resolution of 10% in the center of the crystal. Integral uniformity is 2.1% and differential uniformity is 1.3% after the image is divided by a reference flood image.

ACKNOWLEDGMENTS

This work was supported by Grant No. PO1 CA23417 awarded by the National Cancer Institute, DHHS. In addition, the first author is grateful for fellowship support from SPIE and IBM.

The authors thank Carola Milster, Bruce Moore, Ted Gooley, and David Yocky for help in the preparation of this manuscript, and Lars Selberg, Jyh Chen, Sylvia Rogers, and Tim White for assistance in obtaining the experimental results.

REFERENCES

1. Anger HO. Scintillation camera. *Rev Sci Instrum* 1958; 29:27–33.
2. Milster TD, Selberg LA, Barrett HH, et al. A modular scintillation camera for use in nuclear medicine. *IEEE Trans Nucl Sci* 1984; NS-31:578–580.
3. Genna S, Pang SC, Smith A. Digital scintigraphy: concepts and designs. *IEEE Trans Nucl Sci* 1982; NS-29:558–562.
4. Muehllehner G, Colsher JG, Lewitt RM. A hexagonal bar positron camera: problems and solutions. *IEEE Trans Nuc Sci* 1983; NS-30:652–660.
5. Rogers JG, Saylor DP, Harrop R, Yao XG, Leitao CVM, Pate BD. Design of an efficient position sensitive gamma ray detector for nuclear medicine. *Phys Med Biol* 1986; 31:1061–1090.
6. Rogers WL, Clinthorne NH, Shao L, Koral L. Experimental evaluation of a modular scintillation camera for SPECT. *IEEE Trans Nucl Sci* 1989; NS-36:1122–1126.
7. Burnham C, Bradshaw J, Kaufman D, Chelser D, Brownell GL. One-dimensional scintillation cameras for positron ECT ring detectors. *IEEE Trans Nucl Sci* 1981; NS-28:109–113.
8. Roney TJ, Aarsvold JN, Barrett HH, et al. Modular scintillation cameras: status and applications [Abstract]. 1988; 29:760.
9. Rowe RK, Aarsvold JN, Barrett HH, et al. The design and implementation of modular SPECT imaging systems. In: Todd-Pokropek A, Viergeuer V, eds. *The formation, handling, and evaluation of medical images.* NATO-ASI Series, Springer-Verlag, in press.
10. Selberg LA. Design studies for a modular scintillation camera. MS Thesis, University of Arizona, Tucson, 1984.
11. Barrett HH, Swindell W. *Radiological imaging: the theory of image formation, detection and processing.* New York: Academic Press; 1981:268–278.
12. Murayama H, Tanaka E, Nohara N. A new method for measuring the statistical resolution of scintillation detectors. *Nucl Instrum Methods* 1979; 164:447–451.
13. Milster TD. Design and construction of a modular gamma camera. Ph.D. Dissertation, University of Arizona, Tucson, 1987.
14. Morrison LM, Bruno FP, Mauderli W. Sources of gamma camera image inequalities. *J Nucl Med* 1971; 12:785–791.
15. Milster TD, Selberg LA, Barrett HH, Landesman AL, Seacat III RH. Digital position estimation for the modular scintillation camera. *IEEE Trans Nucl Sci* 1985; NS-32:748–752.
16. Gray RM, Macovski A. Maximum *a posteriori* estimation of position in scintillation cameras. *IEEE Trans Nucl Sci* 1976; NS-23:849–852.
17. Clinthorne NH, Rogers WL, Shao L, Koral KF. A hybrid maximum likelihood position computer for scintillation cameras. *IEEE Trans Nucl Sci* 1987; NS-34:97–101.
18. Anscombe FJ. The transformation of Poisson, binomial and negative-binomial data. *Biometrika* 1948; 35:246–254.
19. Aarsvold JN, Barrett HH, Chen J, et al. Modular scintillation cameras: a progress report. *SPIE Medical Imaging II: Image Formation, Detection, Processing, and Interpretation* 1988; 914:319–325.
20. Performance measurements of scintillation cameras. National Electrical Manufacturers Association 1986; NU-1.